metals

MDPI

Article

Development of a Cr-Ni-V-N Medium Manganese Steel with Balanced Mechanical and Corrosion Properties

Tarek Allam [1,2,*], Xiaofei Guo [1], Simon Sevsek [1], Marta Lipińska-Chwałek [3,4], Atef Hamada [5], Essam Ahmed [2] and Wolfgang Bleck [1]

1 Steel Institute (IEHK), RWTH Aachen University, 52056 Aachen, Germany; xiaofei.guo@iehk.rwth-aachen.de (X.G.); simon.sevsek@iehk.rwth-aachen.de (S.S.); bleck@iehk.rwth-aachen.de (W.B.)
2 Metallurgical and Materials Engineering Department, Suez University, 43528 Suez, Egypt; essam.ahmed@suezuniv.edu.eg
3 Central Facility for Electron Microscopy, RWTH Aachen University, 52074 Aachen, Germany; m.lipinska@fz-juelich.de
4 Forschungszentrum Jülich GmbH, Ernst Ruska-Centre for Microscopy and Spectroscopy with Electrons (ER-C) and Peter Grünberg Institute, Microstructure Research (PGI-5), D-52425 Jülich, Germany
5 Egypt-Japan University of Science and Technology E-JUST, New Borg El-Arab City, 21934 Alexandria, Egypt; atef.hamada@ejust.edu.eg
* Correspondence: tarek.allam@iehk.rwth-aachen.de

Received: 15 May 2019; Accepted: 19 June 2019; Published: 22 June 2019

Abstract: A novel medium manganese (MMn) steel with additions of Cr (18%), Ni (5%), V (1%), and N (0.3%) was developed in order to provide an enhanced corrosion resistance along with a superior strength–ductility balance. The laboratory melted ingots were hot rolled, cold rolled, and finally annealed at 1000 °C for 3 min. The recrystallized single-phase austenitic microstructure consisted of ultrafine grains (~1.3 μm) with a substantial amount of Cr- and V-based precipitates in a bimodal particle size distribution (100–400 nm and <20 nm). The properties of the newly developed austenitic MMn steel X20CrNiMnVN18-5-10 were compared with the standard austenitic stainless steel X5CrNi18-8 and with the austenitic twinning-induced plasticity (TWIP) steel X60MnAl17-1. With a total elongation of 45%, the MMn steel showed an increase in yield strength by 300 MPa and in tensile strength by 150 MPa in comparison to both benchmark steels. No deformation twins were observed even after fracture for the MMn steel, which emphasizes the role of the grain size and precipitation-induced change in the austenite stability in controlling the deformation mechanism. The potentio-dynamic polarization measurements in 5% NaCl revealed a very low current density value of 7.2×10^{-4} mA/cm^2 compared to that of TWIP steel X60MnAl17-1 of 8.2×10^{-3} mA/cm^2, but it was relatively higher than that of stainless steel X5CrNi18-8 of 2.0×10^{-4} mA/cm^2. This work demonstrates that the enhanced mechanical properties of the developed MMn steel are tailored by maintaining an ultrafine grain microstructure with a significant amount of nanoprecipitates, while the high corrosion resistance in 5% NaCl solution is attributed to the high Cr and N contents as well as to the ultrafine grain size.

Keywords: MMn steel X20CrNiMnVN18-5-10; V alloying; corrosion resistance; precipitations; ultrafine grains

1. Introduction

High manganese steels (HMnSs) with the twinning-induced plasticity (TWIP) effect exhibit an excellent combination of high ultimate tensile strength, large uniform elongation, and high work

hardening capacity, which makes them a competitive candidate for a wide range of uses in automotive industry, liquefied natural gas (LNG)-shipbuilding, and the oil and gas industry [1,2]. However, some related material and technological limitations restrict their industrial applications. A processing route consisting of cold rolling followed by a recovery-annealing heat treatment, during which the dislocation density is reduced while previously introduced deformation twins are thermally stable, has been proposed as a solution for the low yield strength of TWIP steels [3,4]. Moreover, the use of microalloying elements has been approached under consideration of the stacking fault energy (SFE), which determines the austenite stability and controls the activation of the secondary deformation mechanism, such as the TWIP effect or deformation induced phase transformation (TRIP—transformation-induced plasticity) in addition to dislocation slip [5]. Due to the high dissolution rate of Mn, TWIP steels exhibit a relatively poor wet corrosion resistance [6,7]. In this regard, different single or combined additions of Cr, Cu, Si, and Al were investigated to enhance the corrosion behavior [8–10]. In a different way to enhance the corrosion resistance and maintain the attractive mechanical properties of TWIP steels, the so-called Fe-Mn-Cr-N TWIP steels have been proposed [11] as a cost-effective substitute for both conventional stainless steel X5CrNi18-8 and HMnS [12]. In that respect, the change in the austenite stability due to N- and Cr- addition has been investigated to design an Fe-Cr-Mn-N system with a stable austenitic microstructure before and after deformation, which can satisfy the corrosion and mechanical requirements of industrial applications [13]. Another barrier to the use of HMnS in different applications is their susceptibility to delayed fracture due to hydrogen embrittlement (HE). Among the various methodologies that have been suggested to alleviate HE in HMnS are Al-addition [14–16], grain refinement [17,18], or the introduction of hydrogen traps, e.g., k-carbides [19]. However, the role of precipitates in improving hydrogen embrittlement is still a matter of discussion [20–22]. Recently, medium manganese steels (MMnSs) with a duplex microstructure have received significant attention due to their excellent mechanical properties and reduced production costs compared to HMnS [23–27].

In light of progress made towards attaining enhanced mechanical and corrosion behavior for TWIP steels and avoiding their material and technological limitations, we designed a new alloying concept with a medium Mn content. This concept is based on the demonstrated excellent corrosion resistance of conventional Fe-Cr-Ni stainless steels and the unique mechanical behavior of TWIP steels, taking into account the austenite stability by adjusting SFE within the TWIP range [28]. In addition, a high V content (1 wt.%) was considered to introduce a significant amount of precipitates to control the grain size. In addition, the impacts of precipitation-strengthening on corrosion resistance, austenite stability, and the activation of additional deformation mechanisms were investigated.

2. Materials and Methods

The alloying concept was designed to develop an austenitic-microstructure MMn steel that can exhibit a high corrosion resistance and a superior strength–ductility balance. Accordingly, C, Mn, Ni, and N were optimized to stabilize the austenite. Cr was added to achieve the envisaged high corrosion resistance, besides the role of N in increasing the pitting resistance. V alloying is considered to increase the mechanical properties by precipitation strengthening and grain refining mechanisms. The chemical composition of the developed MMn steel X20CrNiMnVN18-5-10 is listed in Table 1. A 50 kg heat was ingot-casted and homogenized at 1200 °C for 4 h. Subsequently, the homogenized block was subjected to hot and cold rolling processes to a final thickness of 1.5 mm with a 62.5% cold reduction. The specimens required for different investigations were manufactured before the microstructure was adjusted in a recrystallization annealing treatment at 1000 °C for 3 min in a salt bath. The annealing treatment was designed based on the thermodynamic calculations and precipitation kinetics using Thermo-Calc Software TCFE Steels/Fe-alloys version 9 and MatCalc version 6.02, respectively.

Table 1. Chemical composition in wt.% of the developed medium manganese (MMn) steel as well as the applied benchmark steels.

Elements	C	Si	Mn	Al	Cr	Ni	V	N
MMn X20CrNiMnVN18-5-10	0.17	0.43	10.4	-	17.7	4.7	0.9	0.26
BenchmarkX5CrNi18-8	0.04	0.49	1.2	-	18.0	8.3	-	0.060
Benchmark X60MnAl17-1	0.60	0.06	16.8	1.1	0.6	0.2	0.049	0.008

The developed microstructure was investigated by means of a Zeiss Gemini scanning electron microscopy (SEM) (Carl Zeiss Microscopy GmbH, Jena, Germany) equipped with an energy dispersive X-ray spectrometer (EDS) (Oxford X-Max50, Oxford Instruments, Abingdon, UK) at acceleration voltages of 15 kV and working distances within 10 to 20 mm. The metallographic samples were prepared through the standard preparation route, including cutting and mechanical grinding up to grit 1200 followed by mechanical polishing using 3 µm and 1 µm diamond suspension on a Struers Abrapol-2 (Struers GmbH, Willich, Germany). V2A etching solution was applied to reveal the developed microstructure. The samples used for electron backscatter diffraction (EBSD) measurements were additionally electro-polished at room temperature for 20 s at 22 V using an electrolyte consisting of 700 mL ethanol, 100 mL butyl glycol, and 78 mL 60%-perchloric acid. The EBSD mappings were captured by the EDAX-TSL Hikari detector and analyzed by the OIM-Data Collection-V7.3 software (AMETEK-EDAX Inc., USA). EBSD scans were recorded with a step size of 150 nm applying an acceleration voltage of 15 to 20 kV and a probe current of approximately 30 nA. Evolution of the deformation mechanism was investigated using ex-situ EBSD measurements at the center of the parallel gauge length of tensile samples, which were pulled to different elongation strains. Post-processing of the EBSD measurements was conducted using the HKL Channel 5 software (version 5.12j, Oxford Instruments, Abingdon, UK) and the MATLAB-based MTEX toolbox [29,30] and included the removal of wild spikes and a careful noise reduction, which took at least 5 neighboring data points into account. The precipitation state after recrystallization was identified on electron transparent specimens prepared with the carbon extraction replica method. Conventional bright field imaging of the extracted precipitates was performed using the FEI Tecnai F20 transmission electron microscope (TEM) [31] operated at 200 kV. For detailed characterization of the size distribution and chemical composition of the precipitates, a high angle annular dark field (HAADF) and energy dispersive X-ray (EDX) spectral imaging in a high-resolution Cs probe corrected scanning transmission electron microscope (STEM) FEI Titan G2 80–200 STEM [32] operated at 200 kV was applied. The size of the precipitates was determined from HAADF STEM micrographs of an arbitrarily selected areas of extraction replicas (each 6 µm × 6 µm in size), analyzed with the aid of image processing software, Image J®.

The mechanical properties, namely yield strength (YS), ultimate tensile strength (UTS), and total elongation (El), were evaluated by means of quasi-static tensile testing. The tensile tests were conducted at room temperature with a strain rate of 10^{-3} s^{-1} using a universal tensile testing machine of type Z100 (Zwick/Roell GmbH & Co. KG, Germany) on the recrystallized annealed A30-specimens of 6 mm width and 30 mm parallel gauge length. The strain and force were measured by a videoXtens extensometer attached to the specimen and an Xforce load cell, respectively. Corrosion properties of the MMn steel were evaluated by dynamic polarization measurement in 5% NaCl with a controlled scanning rate of 0.2 mV/s. The corrosion potential, E_{corr}, and corrosion rate, i_{corr}, at the open current potential were determined on the polarization curves by extrapolating the Tafel plots. Mechanical and corrosion values of the developed austenitic MMn steel were compared with two benchmarks, i.e., austenitic stainless steel X5CrNi18-8 and austenitic TWIP steel X60MnAl17-1 (listed in Table 1). The benchmark steels were tested by the same methods used for testing the developed MMn steel in this study.

3. Results

3.1. Thermodynamic and Kinetics Calculations

The recrystallization annealing treatment of the developed MMn steel was designed based on both the thermodynamic calculations of equilibrium phases and the precipitation kinetics. Figure 1a shows the fraction of equilibrium phases based on the actual chemical composition of the MMn steel. It is clear that the austenite phase (FCC_A1) along with carbides ($M_{23}C_6$-type) and nitrides (MN-type) are the expected equilibrium phases by applying an annealing treatment at a temperature of 1000 °C. Figure 1b shows the kinetic of the possible precipitates formed due to annealing at 1000 °C. The kinetics results indicate the formation of the HCP_A3#2 phase (M_2N-type) that starts to saturate within 3 min, while the carbides ($M_{23}C_6$-type) do not tend to form at this temperature.

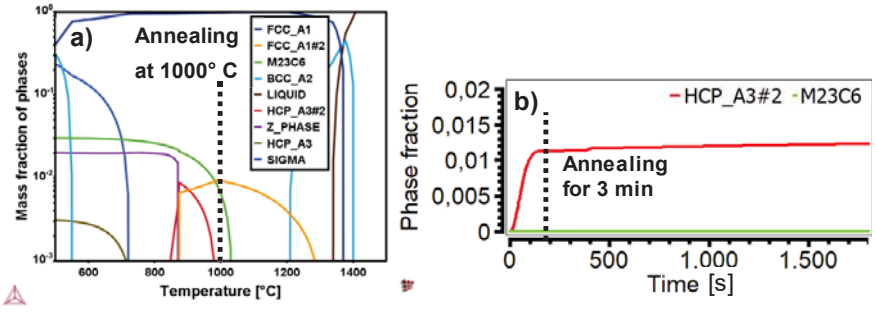

Figure 1. Thermodynamic calculations and precipitation kinetics. (**a**) Mass fraction of equilibrium phases diagram vs. temperature showing that austenite (FCC_A1), carbides ($M_{23}C_6$-type), and nitrides FCC_A1#2 (MN-type) are the equilibrium phases at 1000 °C (Thermo-Calc TCFE 9, MOBFE4). (**b**) Precipitation kinetics at 1000 °C showing the formation of HCP_A3#2 (M2N-type) which comes up to saturation within 3 min (MatCalc version 6.02).

3.2. Microstructure

The thermomechanical processing of the MMn steel resulted in a fine-grained and recrystallized austenitic microstructure containing a considerable amount of precipitates as observed from the SEM image shown in Figure 2a. For the relatively large particles (<150 nm), the EDX-point analysis was applied to reveal their approximate alloying contents. The EDX-spectra represented in Figure 2b shows that the relatively large particles resemble Cr,Fe-rich carbides. The SEM observations and particle analyses are in accordance with the Thermo-Calc equilibrium calculations (Figure 1a). However, the expected precipitation kinetics conducted by MatCalc (Figure 1b) contradicts the formation of Cr-rich carbides during annealing at 1000 °C for 3 min. Instead, it supports the formation of V-rich nitrides. TEM and STEM/EDX investigations confirmed the presence of Cr,Fe-rich carbides (Cr:Fe atomic ratio of 4:1) and Cr,V-rich nitro-carbides (V:Cr atomic ratio of 1:2) as well as V,Cr-rich nitro-carbides (V:Cr atomic ratio of 5:1) with particle sizes of 100 to 150 nm, as indicated in the STEM HAADF image in Figure 2c. Moreover, V,Cr-rich nitro-carbides (V:Cr atomic ratio 5:1) were identified with a relatively larger particle size of ~200 to 400 nm. Additionally, very fine V,Cr-rich nitrides (V:Cr atomic ratio 5:1) with a particle size of <20 nm were observed (in accordance with Thermo-Calc calculations) as depicted in the inset of Figure 2c.

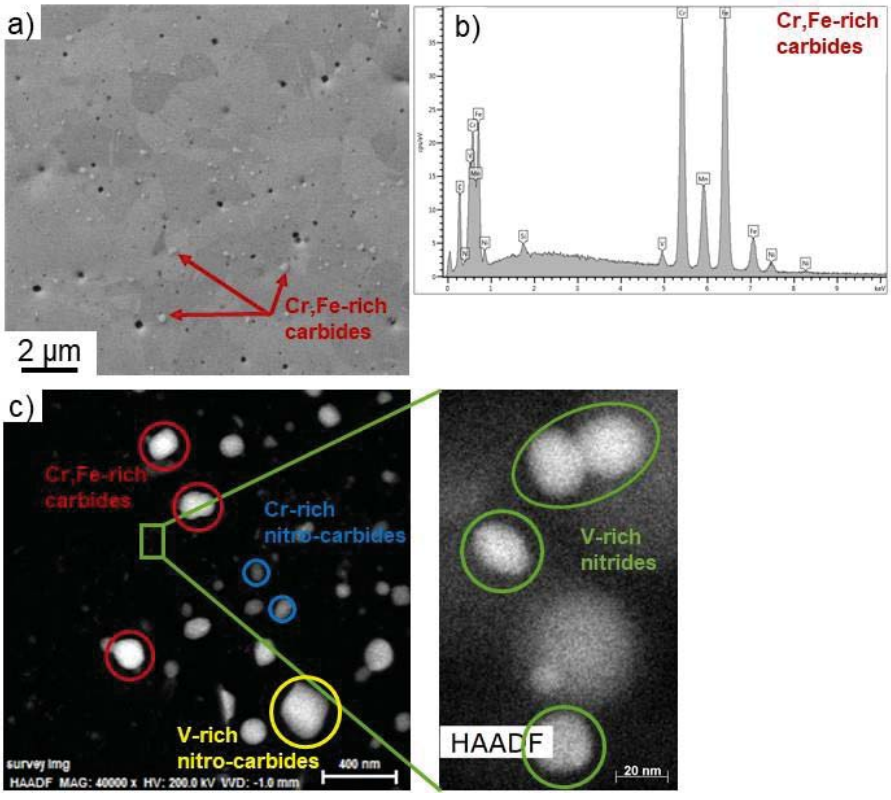

Figure 2. (**a**) SEM micrograph showing the adjusted microstructure after annealing of cold-rolled specimens at 1000 °C for 3 min. In a), the grain boundaries of recrystallized austenitic microstructure are not visible, however, a considerable amount of precipitates can be observed. (**b**) Representative EDX-point analyses for some visible coarse particles. (**c**) STEM HAADF images representing different precipitates with different sizes in the nano-scale. The precipitates were identified with high resolution STEM EDX spectra imaging.

Figure 3 represents the analyses of the EBSD measurements for the MMn steel with and without deformation. The orientation and phase maps in the as-annealed state (in Figure 3a) show that the applied annealing treatment at 1000 °C for 3 minutes resulted in an ultrafine recrystallized austenitic microstructure without a pronounced texture. The average grain size of the adjusted microstructure is around 1.3 µm according to the grain size distribution shown in Figure 3b. The developed austenite microstructure remains mechanically stable after straining to 20% elongation in a tensile irrupted test without any indication for either transformation-induced plasticity (TRIP) nor TWIP effects. However, the specimen pulled until the fracture (with a total elongation of ~48%) showed low amounts of less than 1% ε-martensite (in red) and approximately 2% α'-martensite (in green) at dispersed regions. Deformation twins were not observed at any deformation stage under the applied resolution during EBSD measurements. The corresponding phase maps recorded in the direction of tensile axis for both deformed states, i.e., at 20% elongation and at fracture strain, are shown Figure 3c,d, respectively.

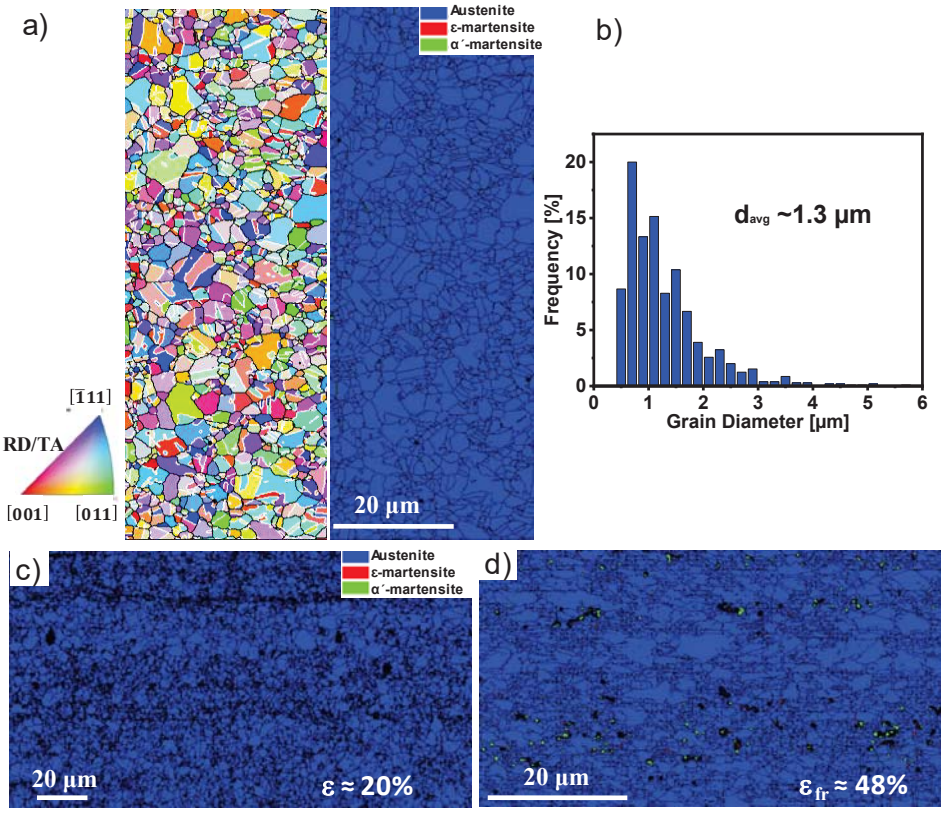

Figure 3. Electron backscatter mappings of the MMn steel annealed at 1000 °C for 3 min. (**a**) The orientation map and the spatial distributions of phases for the developed microstructure without deformation. RD and TA denote the rolling direction and tensile axis, respectively. (**b**) Grain size distribution and average grain size determined by the line-intercept method considering the annealing twins. (**c**) and (**d**) The spatial distribution of phases (austenite in blue, ε-martensite in red, α´-martensite in green, and black not indexed) formed at 20% elongation and at fracture strain, respectively.

3.3. Mechanical Properties

Quasi-static tensile properties, namely YS, UTS, and total El, for the MMn steel were compared to benchmark stainless steel X5CrNi18-8 and TWIP steel X60MnAl17-1 as depicted in Figure 4. According to the engineering stress–strain curves and the corresponding inset bar-chart in Figure 4a, the MMn steel shows higher YS and UTS values and a relatively lower total El that is still reasonably high for cold formability applications. The applied annealing treatment led to YS and UTS values of ~600 and 975 MPa, respectively, along with a total El of more than 45%. This demonstrates a jump in YS and UTS of approximately 300 and more than 150 MPa, respectively, compared to their counterparts of benchmark steels. Figure 4b represents the corresponding work hardening rate (WHR) calculated from the tensile test data. It is worthy to note that besides the higher YS and UTS values of the MMn steel, the WHR is also higher than both benchmark steels up to true strain values of ~0.16 and 0.25, respectively. The MMn steel exhibits an initial WHR (measured at 0.02) of ~3.4 GPa, which is higher than those of other benchmark steels. This initial high WHR decreases gradually and reached the same WHR of X5CrNi18-8 and X60MnAl17-1 benchmark steels at true stress values of ~1.1 and 1.2 GPa,

respectively. Moreover, the WHR decreases at a slightly lower rate after around >0.18 true strain (>20% elongation) as can be realized from its slope illustrated by black dotted lines.

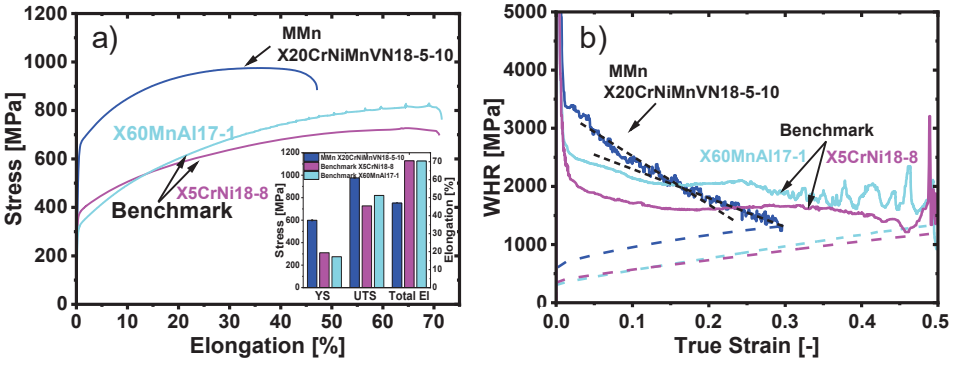

Figure 4. Tensile properties of the MMn steel X20CrNiMnVN18-5-10 in comparison to the benchmark stainless steel X5CrNi18-8 and TWIP steel X60MnAl17-1. (**a**) Engineering stress–strain curves with a bar chart showing the achievable strength and ductility levels. (**b**) The work hardening rate (WHR) curves.

3.4. Corrosion Properties

The corrosion properties of MMn steel were evaluated and compared to the benchmark steels. Figure 5a displays the results of the dynamic polarization measurements, which were carried out to evaluate the corrosion properties in terms of the open current potential (E_{corr}) and corrosion current density (i_{corr}) of the MMn steel compared to the benchmark steels. Obviously, the MMn steel exhibits a distinctively higher positive E_{corr} value of −299 mV_{SCE} than that observed for TWIP steel X60MnAl17-1 of −658 mV_{SCE}, while stainless steel X5CrNi18-8 shows the highest positive E_{corr} value of −144 mV_{SC}. Moreover, the i_{corr} (determined by Tafel lines calculations) shows a very low value of 7.2×10^{-4} mA/cm^2 compared to TWIP steel X60MnAl17-1 with a value of 8.2×10^{-3} mA/cm^2, but it is slightly higher than that of stainless steel X5CrNi18-8 with a value of 2.0×10^{-4} mA/cm^2. The bar chart in Figure 5b points out the corrosion current ratio (CCR) of each tested grade with respect to the benchmark stainless steel X5CrNi18-8. The calculated CCR values demonstrate that the corrosion behavior of MMn steel is superior to the TWIP steel X60MnAl17-1, while it is lower but still could be compared to the stainless steel X5CrNi18-8.

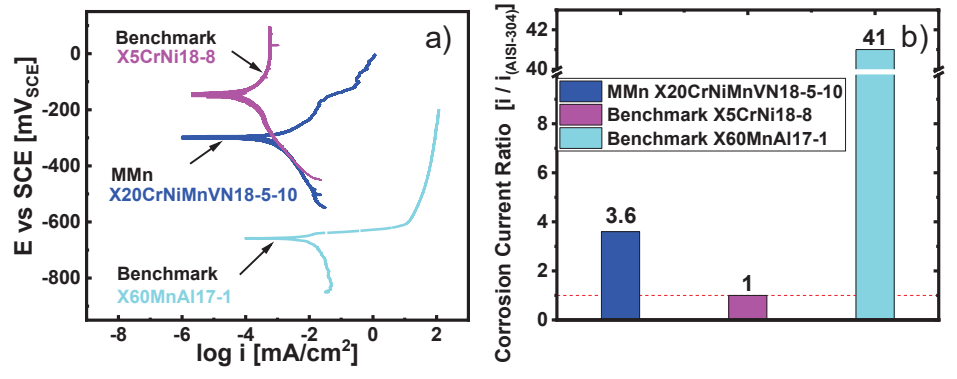

Figure 5. Dynamic polarization measurements in 5% NaCl showing the corrosion properties of the MMn steel compared to the benchmark steels. (**a**) Recorded polarization curves. (**b**) The corrosion current ratio with respect to the benchmark stainless steel X5CrNi18-8.

4. Discussion

4.1. Interplay among Different Strengthening Effects Induced by V Alloying

The developed ultrafine grain microstructure containing large Cr,Fe-rich carbides, Cr,V-rich nitro-carbides, V,Cr-rich nitro-carbides, and very fine V,Cr-rich nitrides shows superior strength–ductility balance, which emphasizes the synergetic effect of the nanoprecipitates and the ultrafine grains on controlling the strength level and hardening mechanism. The substantial increase in YS of MMn steel compared to the benchmark steels is attributed to the Ashby–Orowan effect for precipitation-strengthening, Hall–Petch effect for grain-size strengthening, solid–solution, and dislocation strengthening induced by V alloying. Since the formed precipitates are of different sizes, they will contribute differently to the increment in yield strength. According to the Ashby–Orowan relationship [33], the increment in yield strength increases as the size of particles decreases. Based on the size distribution analysis of the formed precipitates, >80% of the whole particles are smaller than 50 nm, which emphasizes the major role of the precipitation-strengthening mechanism.

There are additional effects caused by V alloying that act in a close interplay with nanoprecipitates on improving the YS of the MMn steel. As observed from the grain size distribution in Figure 3b, the annealing treatment at 1000 °C for 3 min resulted in a recrystallized and ultrafine grained microstructure that contributes to the increase in yield strength, which is commonly referred to as the Hall–Petch effect [34,35]. In addition to Ashby–Orowan and Hall–Petch effects, solid–solution strengthening due to the dissolved V and N solutes contributes to the YS value of the MMn steel. As can be noted from Figure 6, the thermodynamic equilibrium austenite at the applied annealing temperature still contains around 0.2 and 0.1 wt.% of dissolved V and N solutes, respectively. Norström [36] demonstrated a significant increase in yield strength of N-alloyed stainless steel due to the solid solution-hardening effect. Moreover, Werner [37] established that the increment in yield strength due to solid–solution strengthening of N-alloyed stainless steel was considerably higher than that achieved by grain refinement at the same amount of N.

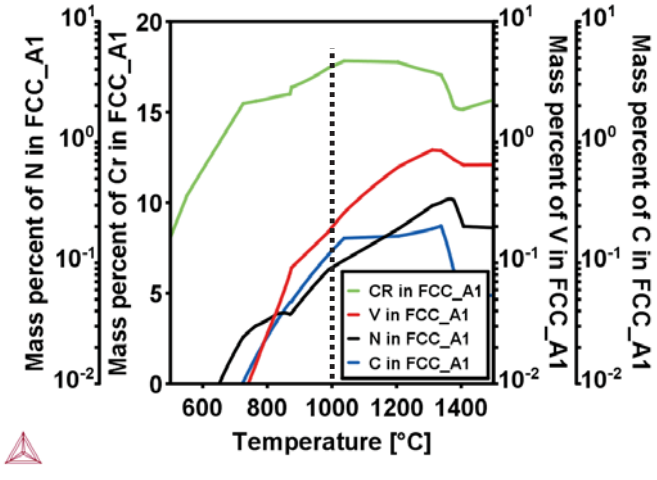

Figure 6. The change in equilibrium solubility in the mass percent of C, N, Cr, and V in austenite with temperature for the MMn steel.

Furthermore, the formation of precipitates is considered to be responsible for the suppression of the complete dislocation annihilation during annealing and hence increasing the yield strength via the dislocation hardening effect. In the same context for V-alloyed MMn steel, Hu et al. [38] reported a small increment in yield strength due to grain refinement, however, they emphasized the role of

VC precipitates and dislocation hardening in increasing the yield strength. The observed increase in yield strength due to V alloying is in agreement with several studies [39–42] that reported solely the pronounced effect of V precipitates; however, the current study emphasizes additional effects, such as grain–boundary, solid–solution, and dislocation strengthening.

4.2. Strain Hardening Behavior

Although the SFE for the MMn steel was adjusted in the TWIP range, it shows a high WHR at early deformation stages with a gradual decrease until fracture, which is quite different from the common WHR of conventional TWIP steels. Despite the gradual decrease in its WHR, the MMn steel maintains higher values of WHR than those of benchmark steels until around 20% elongation, thus allowing for a superior UTS value as observed in Figure 4. However, the gradual decrease in its WHR facilitates the early strain localization and results in a relatively lower but still comparable total elongation to the benchmark steels.

The high WHR at early deformation stages can be attributed to the grain refinement effect. However, the suppression of deformation twin formation results in a continuous drop in WHR. The austenite to martensite transformation is considered the reason for the slight decrease in the drop rate of WHR at later deformation stages (higher than 20% elongation) as observed from the EBSD maps in Figure 3d. Several studies emphasized the profound effect of grain refinement on the restriction of deformation twins. Ueji et al. [43] studied the twinning behavior of different high Mn austenitic steels with various mean grain sizes (1.8, 7.2, and 49.6 μm) and reported that the deformation twinning is strongly inhibited by grain refinement. Rahman et al. [44] reported the increase in twin nucleation stress with decreasing grain size. Lee et al. [45] attributed the increase in twinning stress to the suppression of dislocation activity and movement of partial dislocations by interaction with a high dislocation density in fine grain sized specimens. In the same regard, Gutierrez-Urrutia et al. [46,47] ascribed the increase in twinning stress resistance to the activation of multiple slip propagation, which is a perquisite to deformation twin formation. In general, the work hardening rate is related to the grain size, dislocation density, and the active deformation mechanism defined mostly by SFE [48–51]. Since the microstructure of the MMn steel contains a considerable amount of precipitates, the local chemical changes in the precipitates surroundings, especially C and N, will lead eventually to a decrease in the SFE and hence the possibility of austenite to martensite transformation as observed in Figure 3d. This has also been reported by Yen et al. [42].

4.3. Enhanced Corrosion Resistance

The potentiodynamic polarization measurements of the MMn steel demonstrate an enhanced corrosion resistance, which is superior to that of TWIP steel X60MnAl17-1 but still lower than that of stainless steel X5CrNi18-8. This enhanced corrosion resistance over the TWIP steel can be ascribed to the high Cr content. The thermodynamic equilibrium Cr content in austenite does not decrease significantly by the formation of precipitates at 1000 °C as shown in Figure 6. Nevertheless, the formed precipitates allow for the creation of corrosion cells that contribute detrimentally to corrosion resistance and passivation behavior of the MMn steel. Therefore, the lower corrosion resistance and the apparent increase in i_{corr} compared to stainless steel X5CrNi18-8 can be accounted for the formed precipitates. Although the corrosion current ratio of the MMn steel with respect to X5CrNi18-8 is 3.6, it was expected to be higher than this ratio due to precipitation, since Yan et al. [52] found that the precipitates of chromium-rich carbides in 316 L stainless steel resulted in severe pitting corrosion. However, in the current study, it seems that the grain refinement plays a significant role in enhancing the pitting resistance, in addition to the role of N. The pitting resistance equivalent number (PREN), which is a predictive measurement for the resistance of stainless steels to localized pitting corrosion based on their chemical composition [53], increases with N addition as indicated in Equation (1). The PREN number is 21.4 for the MMn steel, while 19.8 for the stainless steel X5CrNi18-8. Moreover, Hamada et al. [54] reported a significant improvement in the corrosion resistance of 301 LN as a result of grain

refinement. It is well established that the segregation of impurities or the formation of chromium nitrides on the grain boundaries of stainless steel is more severe in a coarse-grained structure than in an ultrafine-grained structure, which is more homogeneous and has a smoother structure. Furthermore, the compactness and stability of the passive film formed on nano/submicron-grained structure is significantly increased [55,56]:

$$PREN = 1 \times \%Cr + 3.3 \times \%Mo + 16 \times \%N. \quad (1)$$

The current study demonstrates that V alloying resulted in a synergetic effect of precipitates and ultrafine grain size on both mechanical properties and corrosion behavior for the MMn steel. Indeed, the designed alloy concept provides the possibility to overcome some HMnS limitations, such as low yield strength values, poor corrosion resistance, and processing problems due to the high Mn content. Furthermore, the preliminary investigations on its hydrogen embrittlement behavior showed a significant improvement compared to conventional TWIP steels, even those Al-alloyed. However, a proper adjustment of the type and amount of precipitates could further enhance the corrosion resistance mechanical behavior of the MMn. This requires deeper understanding for the nature of the interaction between precipitates and other micro- and nanostructure defects.

5. Conclusions

The main aim of the present study was to develop a novel austenitic MMn steel X20CrNiMnVN18-5-10 that exhibits an enhanced corrosion resistance and a superior strength–ductility balance. The alloying additions were optimized to attain an ultrafine austenitic microstructure with a significant amount of nanoprecipitates. Alloying with V (1 wt.%) and N (0.3 wt.%) has been considered for precipitation and grain size control. The corrosion resistance and mechanical properties of the MMn steel were investigated and compared to their counterparts of two benchmark steels, i.e., austenitic stainless steel X5CrNi18-8 and austenitic TWIP steel X60MnAl17-1. Based on the findings, the following conclusions can be drawn:

1. Recrystallization annealing treatment at 1000 °C for 3 min resulted in an ultrafine austenitic microstructure with an average grain size of ~1.3 μm containing a considerable amount of V- and Cr-based precipitates in a bimodal particle size distribution (100–400 nm and <20 nm). More than 80% of the precipitates are smaller than 50 nm.
2. The alloying concept (especially the high V and N contents) results in a high yield strength of ~600 MPa via an interplay among different mechanisms, namely the Ashby–Orowan effect, Hall–Petch effect, solid–solution, and dislocation strengthening.
3. Although the work hardening rate (WHR) at early deformation stages is very high (3.4 GPa), the suppression of deformation twin formation by ultrafine grains until fracture resulted in a continuous drop in WHR. The slope of the WHR decreases at high strains (>20%) due to the austenite to martensite transformation.
4. The enhanced corrosion resistance of the newly developed MMn steel is attributed to the high Cr and N contents even after precipitation. It seems that the ultrafine grain microstructure plays an important role in improving the corrosion resistance despite the detrimental effect of precipitates.

Author Contributions: T.A. designed, performed, analyzed, and interpreted the experimental data, such as heat treatment, SEM, tensile tests, and mechanical properties. X.G. performed the corrosion tests, precipitate size measurements, and analyzed the data. M.L.-C. performed the TEM and STEM/EDX investigations and processed the data. S.S. performed the EBSD measurements and analyzed the data. A.H. and E.A. designed and produced the material. W.B. contributes to ideas and intensive discussions. T.A. wrote the original draft. All authors contributed to interpretation of the results and writing the final version of the manuscript.

Acknowledgments: A.H. and E.A. gratefully acknowledge the STDF-Egypt for supporting the melt production. T.A. expresses his gratitude to the DAAD for the personal financial support. DFG within the Collaborative Research Center (SFB) 761 is appreciated for supporting the processing and testing the developed steel grade.

Conflicts of Interest: The authors declare no conflict of interest.

References

1. Grässel, O.; Krüger, L.; Frommeyer, G.; Meyer, L.W. High strength Fe–Mn–(Al, Si) TRIP/TWIP steels development—Properties—Application. *Int. J. Plast.* **2000**, *16*, 1391–1409. [CrossRef]
2. de Cooman, B.C.; Estrin, Y.; Kim, S.K. Twinning-induced plasticity (TWIP) steels. *Acta Mater.* **2018**, *142*, 283–362. [CrossRef]
3. Bouaziz, O.; Allain, S.; Scott, C.P.; Cugy, P.; Barbier, D. High manganese austenitic twinning induced plasticity steels: A review of the microstructure properties relationships. *Curr. Opin. Solid State Mater. Sci.* **2011**, *15*, 141–168. [CrossRef]
4. Haase, C.; Ingendahl, T.; Güvenç, O.; Bambach, M.; Bleck, W.; Molodov, D.A.; Barrales-Mora, L.A. On the applicability of recovery-annealed Twinning-Induced Plasticity steels: Potential and limitations. *Mater. Sci. Eng. A* **2016**, *649*, 74–84. [CrossRef]
5. Dumay, A.; Chateau, J.-P.; Allain, S.; Migot, S.; Bouaziz, O. Influence of addition elements on the stacking-fault energy and mechanical properties of an austenitic Fe–Mn–C steel. *Mater. Sci. Eng. A* **2008**, *2008*, 184–187. [CrossRef]
6. Grajcar, A. Corrosion resistance of high-Mn austenitic steels for the automotive industry. In *Corrosion Resistance*; InTech: Rijeka, Croatia, 2012.
7. Kannan, M.B.; Raman, R.S.; Khoddam, S. Comparative studies on the corrosion properties of a Fe–Mn–Al–Si steel and an interstitial-free steel. *Corros. Sci.* **2008**, *50*, 2879–2884. [CrossRef]
8. Zhang, Y.S.; Zhu, X.M. Electrochemical polarization and passive film analysis of austenitic Fe–Mn–Al steels in aqueous solutions. *Corros. Sci.* **1999**, *41*, 1817–1833. [CrossRef]
9. Zhang, Y.S.; Zhu, X.M.; Liu, M.; Che, R.X. Effects of anodic passivation on the constitution, stability and resistance to corrosion of passive film formed on an Fe-24Mn-4Al-5Cr alloy. *Appl. Surf. Sci.* **2004**, *222*, 89–101. [CrossRef]
10. Dieudonné, T.; Marchetti, L.; Wery, M.; Miserque, F.; Tabarant, M.; Chêne, J.; Allely, C.; Cugy, P.; Scott, C.P. Role of copper and aluminum on the corrosion behavior of austenitic Fe–Mn–C TWIP steels in aqueous solutions and the related hydrogen absorption. *Corros. Sci.* **2014**, *83*, 234–244. [CrossRef]
11. Toor, I.-U.-H.; Hyun, P.J.; Kwon, H.S. Development of high Mn–N duplex stainless steel for automobile structural components. *Corros. Sci.* **2008**, *50*, 404–410. [CrossRef]
12. Di Schino, A.; Kenny, J.M.; Mecozzi, M.G.; Barteri, M. Development of high nitrogen, low nickel, 18%Cr austenitic stainless steels. *J. Mater. Sci.* **2000**, *35*, 4803–4808. [CrossRef]
13. Mosecker, L.; Saeed-Akbari, A. Nitrogen in chromium–manganese stainless steels: A review on the evaluation of stacking fault energy by computational thermodynamics. *Sci. Technol. Adv. Mater.* **2013**, *14*, 33001. [CrossRef] [PubMed]
14. de Cooman, B.C.; Chin, K.-G.; Kim, J. High Mn TWIP Steels for Automotive Applications. In *New Trends and Developments in Automotive System Engineering*; Chiaberge, M., Ed.; InTech: Bratislava, Slovakia, 2011; ISBN 978-953-307-517-4.
15. Kim, Y.; Kang, N.; Park, Y.; Choi, I.; Kim, G.; Kim, S.; Cho, K. Effects of the strain induced martensite transformation on the delayed fracture for Al-added TWIP steel. *J. Korean Inst. Met. Mater.* **2008**, *46*, 780–787.
16. Koyama, M.; Akiyama, E.; Tsuzaki, K. Hydrogen Embrittlement in Al-added Twinning-induced Plasticity Steels Evaluated by Tensile Tests during Hydrogen Charging. *ISIJ Int.* **2012**, *52*, 2283–2287. [CrossRef]
17. Zan, N.; Ding, H.; Guo, X.; Tang, Z.; Bleck, W. Effects of grain size on hydrogen embrittlement in a Fe-22Mn-0.6C TWIP steel. *Int. J. Hydrogen Energy* **2015**, *40*, 10687–10696. [CrossRef]
18. Park, I.-J.; Lee, S.-M.; Jeon, H.-H.; Lee, Y.-K. The advantage of grain refinement in the hydrogen embrittlement of Fe–18Mn–0.6C twinning-induced plasticity steel. *Corros. Sci.* **2015**, *93*, 63–69. [CrossRef]
19. Timmerscheidt, T.; Dey, P.; Bogdanovski, D.; von Appen, J.; Hickel, T.; Neugebauer, J.; Dronskowski, R. The Role of κ-Carbides as Hydrogen Traps in High-Mn Steels. *Metals* **2017**, *7*, 264. [CrossRef]
20. Ooi, S.W.; Ramjaun, T.I.; Hulme-Smith, C.; Morana, R.; Drakopoulos, M.; Bhadeshia, H.K.D.H. Designing steel to resist hydrogen embrittlement Part 2—Precipitate characterisation. *Mater. Sci. Technol.* **2018**, *34*, 1747–1758. [CrossRef]

21. Zhang, Z.; Moore, K.L.; McMahon, G.; Morana, R.; Preuss, M. On the role of precipitates in hydrogen trapping and hydrogen embrittlement of a nickel-based superalloy. *Corros. Sci.* **2019**, *146*, 58–69. [CrossRef]
22. Takahashi, J.; Kawakami, K.; Kobayashi, Y. Origin of hydrogen trapping site in vanadium carbide precipitation strengthening steel. *Acta Mater.* **2018**, *153*, 193–204. [CrossRef]
23. Suh, D.W.; Ryu, J.H.; Joo, M.S.; Yang, H.S.; Lee, K.; Bhadeshia, H.K.D.H. Medium-Alloy Manganese-Rich Transformation-Induced Plasticity Steels. *Metall. Mater. Trans. A* **2013**, *44*, 286–293. [CrossRef]
24. Lee, Y.-K.; Han, J. Current opinion in medium manganese steel. *Mater. Sci. Technol.* **2014**, *31*, 843–856. [CrossRef]
25. Sun, B.; Ding, R.; Brodusch, N.; Chen, H.; Guo, B.; Fazeli, F.; Ponge, D.; Gauvin, R.; Yue, S. Improving the ductility of ultrahigh-strength medium Mn steels via introducing pre-existed austenite acting as a "reservoir" for Mn atoms. *Mater. Sci. Eng. A* **2019**, *749*, 235–240. [CrossRef]
26. Sun, B.; Fazeli, F.; Scott, C.; Brodusch, N.; Gauvin, R.; Yue, S. The influence of silicon additions on the deformation behavior of austenite-ferrite duplex medium manganese steels. *Acta Mater.* **2018**, *148*, 249–262. [CrossRef]
27. Kaar, S.; Schneider, R.; Krizan, D.; Béal, C.; Sommitsch, C. Influence of the Quenching and Partitioning Process on the Transformation Kinetics and Hardness in a Lean Medium Manganese TRIP Steel. *Metals* **2019**, *9*, 353. [CrossRef]
28. Hamada, A.; Juuti, T.; Khosravifard, A.; Kisko, A.; Karjalainen, P.; Porter, D.; Kömi, J. Effect of silicon on the hot deformation behavior of microalloyed TWIP-type stainless steels. *Mater. Des.* **2018**, *154*, 117–129. [CrossRef]
29. Hielscher, R.; Schaeben, H. A novel pole figure inversion method: Specification of the MTEX algorithm. *J. Appl. Cryst.* **2008**, *41*, 1024–1037. [CrossRef]
30. Bachmann, F.; Hielscher, R.; Schaeben, H. Texture Analysis with MTEX—Free and Open Source Software Toolbox. *SSP* **2010**, *160*, 63–68. [CrossRef]
31. Luysberg, M.; Heggen, M.; Tillmann, K. FEI Tecnai G2 F20. *JLSRF* **2016**, *2*. [CrossRef]
32. Kovács, A.; Schierholz, R.; Tillmann, K. FEI Titan G2 80-200 CREWLEY. *JLSRF* **2016**, *2*. [CrossRef]
33. Gladman, T. Precipitation hardening in metals. *Mater. Sci. Technol.* **1999**, *15*, 30–36. [CrossRef]
34. Hansen, N. Hall–Petch relation and boundary strengthening. *Scr. Mater.* **2004**, *51*, 801–806. [CrossRef]
35. Hall, E.O. The Deformation and Ageing of Mild Steel: III Discussion of Results. *Proc. Phys. Soc. Sect. B* **1951**, *64*, 747–753. [CrossRef]
36. Norström, L.-Å. The influence of nitrogen and grain size on yield strength in Type AISI 316L austenitic stainless steel. *Met. Sci.* **1977**, *11*, 208–212. [CrossRef]
37. Werner, E. Solid solution and grain size hardening of nitrogen-alloyed austenitic steels. *Mater. Sci. Eng. A* **1988**, *101*, 93–98. [CrossRef]
38. Hu, B.; He, B.B.; Cheng, G.J.; Yen, H.W.; Luo, H.W.; Huang, M.X. Super-High-Strength and Formable Medium Mn Steel Manufactured by Warm Rolling Process. 23 March 2019. Available online: https://ssrn.com/abstract=3358845 (accessed on 26 April 2019).
39. Yazawa, Y.; Furuhara, T.; Maki, T. Effect of matrix recrystallization on morphology, crystallography and coarsening behavior of vanadium carbide in austenite. *Acta Mater.* **2004**, *52*, 3727–3736. [CrossRef]
40. Atasoy, Ö.A.; Özbaysal, K.; Inal, O.T. Precipitation of vanadium carbides in 0.8% C-13% Mn-1% V austenitic steel. *J. Mater. Sci.* **1989**, *24*, 1393–1398. [CrossRef]
41. Sohn, S.S.; Song, H.; Jo, M.C.; Song, T.; Kim, H.S.; Lee, S. Novel 1.5 GPa-strength with 50%-ductility by transformation-induced plasticity of non-recrystallized austenite in duplex steels. *Sci. Rep.* **2017**, *7*, 1255. [CrossRef]
42. Yen, H.-W.; Huang, M.; Scott, C.P.; Yang, J.-R. Interactions between deformation-induced defects and carbides in a vanadium-containing TWIP steel. *Scr. Mater.* **2012**, *66*, 1018–1023. [CrossRef]
43. Ueji, R.; Tsuchida, N.; Terada, D.; Tsuji, N.; Tanaka, Y.; Takemura, A.; Kunishige, K. Tensile properties and twinning behavior of high manganese austenitic steel with fine-grained structure. *Scr. Mater.* **2008**, *59*, 963–966. [CrossRef]
44. Rahman, K.M.; Vorontsov, V.A.; Dye, D. The effect of grain size on the twin initiation stress in a TWIP steel. *Acta Mater.* **2015**, *89*, 247–257. [CrossRef]

45. Lee, S.-I.; Lee, S.-Y.; Han, J.; Hwang, B. Deformation behavior and tensile properties of an austenitic Fe-24Mn-4Cr-0.5C high-manganese steel: Effect of grain size. *Mater. Sci. Eng. A* **2019**, *742*, 334–343. [CrossRef]
46. Gutierrez-Urrutia, I.; Zaefferer, S.; Raabe, D. The effect of grain size and grain orientation on deformation twinning in a Fe–22 wt.% Mn–0.6 wt.% C TWIP steel. *Mater. Sci. Eng. A* **2010**, *527*, 3552–3560. [CrossRef]
47. Gutierrez-Urrutia, I.; Raabe, D. Grain size effect on strain hardening in twinning-induced plasticity steels. *Scr. Mater.* **2012**, *66*, 992–996. [CrossRef]
48. Bouaziz, O.; Allain, S.; Scott, C. Effect of grain and twin boundaries on the hardening mechanisms of twinning-induced plasticity steels. *Scr. Mater.* **2008**, *58*, 484–487. [CrossRef]
49. Idrissi, H.; Renard, K.; Ryelandt, L.; Schryvers, D.; Jacques, P.J. On the mechanism of twin formation in Fe–Mn–C TWIP steels. *Acta Mater.* **2010**, *58*, 2464–2476. [CrossRef]
50. Saeed-Akbari, A.; Mosecker, L.; Schwedt, A.; Bleck, W. Characterization and Prediction of Flow Behavior in High-Manganese Twinning Induced Plasticity Steels: Part I. Mechanism Maps and Work-Hardening Behavior. *Metall. Mater. Trans. A* **2012**, *43*, 1688–1704. [CrossRef]
51. Renard, K.; Jacques, P.J. On the relationship between work hardening and twinning rate in TWIP steels. *Mater. Sci. Eng. A* **2012**, *542*, 8–14. [CrossRef]
52. Yan, S.; Shi, Y.; Liu, J.; Ni, C. Effect of laser mode on microstructure and corrosion resistance of 316L stainless steel weld joint. *Opt. Laser Technol.* **2019**, *113*, 428–436. [CrossRef]
53. Okada, T.; Hashino, T. A contribution to the kinetic theory of pitting corrosion. *Corros. Sci.* **1977**, *17*, 671–689. [CrossRef]
54. Hamada, A.S.; Karjalainen, L.P.; El-Zeky, M.A. Effect of anodic passivation on the corrosion behaviour of Fe-Mn-Al steels in 3.5% NaCl. In *Passivation of Metals and Semiconductors, and Properties of Thin Oxide Layers*; Elsevier: Amsterdam, The Netherlands, 2006; pp. 77–82.
55. Hamada, A.S.; Karjalainen, L.P.; Somani, M.C. Electrochemical corrosion behaviour of a novel submicron-grained austenitic stainless steel in an acidic NaCl solution. *Mater. Sci. Eng. A* **2006**, *431*, 211–217. [CrossRef]
56. Jinlong, L.; Hongyun, L. Comparison of corrosion properties of passive films formed on phase reversion induced nano/ultrafine-grained 321 stainless steel. *Appl. Surf. Sci.* **2013**, *280*, 124–131. [CrossRef]



© 2019 by the authors. Licensee MDPI, Basel, Switzerland. This article is an open access article distributed under the terms and conditions of the Creative Commons Attribution (CC BY) license (http://creativecommons.org/licenses/by/4.0/).